Powder Technology 291 (2016) 284–298

Contents lists available at ScienceDirect

Powder Technology

journal homepage: www.elsevier.com/locate/powtec

Numerical and experimental study of pulse-jet cleaning in fabric filters

B.O. Andersen [a,*], N.F. Nielsen [a], J.H. Walther [b,c]

[a] FLSmidth A/S, Airtech, Vigerslev Allé 77, 2500 Valby, Denmark
[b] DTU Mechanical Engineering, Technical University of Denmark, Nils Koppels Alle, Building 403, room 216, 2800 Kgs. Lyngby, Denmark
[c] Computational Science and Engineering Laboratory, ETH Zurich, Clausiusstrasse 33, CH-8092, Zurich, Switzerland

ARTICLE INFO

Article history:
Received 30 July 2015
Received in revised form 25 November 2015
Accepted 21 December 2015
Available online 30 December 2015

Keywords:
Computational fluid dynamics
Fabric filter
Baghouse
Pulse-jet cleaning
Low-pressure cleaning
Design optimisation

ABSTRACT

Pulse-jet cleaning and understanding of the complex physics are essential when designing fabric filters used for air pollution control. Today, low-pressure cleaning is of particular interest due to demand for reduced compressed air consumption. Pulse-jet cleaned fabric filters have been studied for many years by experimental investigation and to a limited extent by Computational Fluid Dynamics (CFD). The majority of the studies have focused on high-pressure cleaning systems, and the CFD models presented are so far two-dimensional (2D). In the work presented here, pulse-jet cleaning of low-pressure fabric filters (2 bar) is studied using a full three-dimensional (3D) CFD model. Experimental results obtained in a pilot-scale test filter with 28 bags, in length of 10 m and in general full-scale dimensions of the cleaning system are used to verify the reliability of the present CFD model. The validated CFD model reveals the strong compressible effects, a highly transient behaviour, the formation of compressible vortex rings and the shock cell phenomenon within the overexpanded supersonic jet. The cleaning nozzles and venturi design aid or oppose the pulse-pressure within the bags, and this plays an important role in the resulting efficiency of removing the dust layer from the bags. The CFD simulation shows that the traditional straight-bore nozzles provide substantial misalignment of the jet, and the add-on nozzle design offers only limited improvement. Further, the need for venturis in low-pressure filters and the importance of optimising the venturi design are demonstrated. The working principle of the venturi is to restrict backflow which is detrimental to the pressure rise in the bags. Reducing the venturi throat diameter is shown to reduce backflow and improve the pulse-pressure.

1. Introduction

Pulse-jet cleaned fabric filters are commonly used for air pollution control in many industries, e.g. power production and mining. Dust transported by the flue gas is collected on the external surface of the fabric bag, thereby forming a so-called 'dust cake'. Periodic removal of the dust cake is required due to the continuous build-up of dust. Pulse-jet cleaning is widely used for this purpose as it enables frequent cleaning whilst the filter is operating.

In pulse-jet cleaning, a short pulse (50–150 ms) of compressed air is released by a valve and distributed in a purge tube to multiple nozzles (Fig. 1). Each nozzle is directed towards a venturi placed above the open end of a single bag. The compressed air expands through the nozzle, thereby forming a pulse-jet of primary air. In the near-field region around the pulse-jet, secondary air entrains the pulse-jet as it travels towards the venturi (Fig. 2). The pulse-jet acts in countercurrent direction to the flow of flue gas during normal filter operation (Fig. 3). In cleaning mode, the pulse-jet travels through the venturi and into the bag where the flow reversal and high resistance in the fabric cause an internal pressure increase called the pulse pressure. As a result, the bag is briefly inflated and the dust cake is removed (Fig. 3 right).

In recent years, interest in low-pressure pulse-jet cleaning has increased in the search for reduced energy consumption. Low-pressure filters operate at a tank pressure of 2–3 bar gauge, whereas traditional high-pressure filters operate at much higher pressure, typically 4–7 bar gauge. This relatively new technology is expected to introduce challenges not found in traditional high-pressure systems. Of particular interest is the potential axial misalignment between pulse-jet and venturi/bag.

In low-pressure filters, the lower density of the compressed air is expected to cause higher axial velocity in the purge tube and therefore increased jet misalignment.

Understanding the jet behaviour and the interaction with the venturi and bag is crucial to design effective pulse-jet cleaned fabric filters. The introduction of low-pressure filters poses an even greater challenge to engineers, requiring a detailed insight into the highly dynamic fluid flow. Obtaining this valuable information is difficult through conventional methods relying on physical measurements, which often fall short in terms of spatial as well as temporal resolution. Computational Fluid Dynamics (CFD) is highly suited for this purpose as it offers the

* Corresponding author.
E-mail address: bjoa@flsmidth.com (B.O. Andersen).
URL: http://www.flsmidthairtech.com (B.O. Andersen).

http://dx.doi.org/10.1016/j.powtec.2015.12.028
0032-5910/

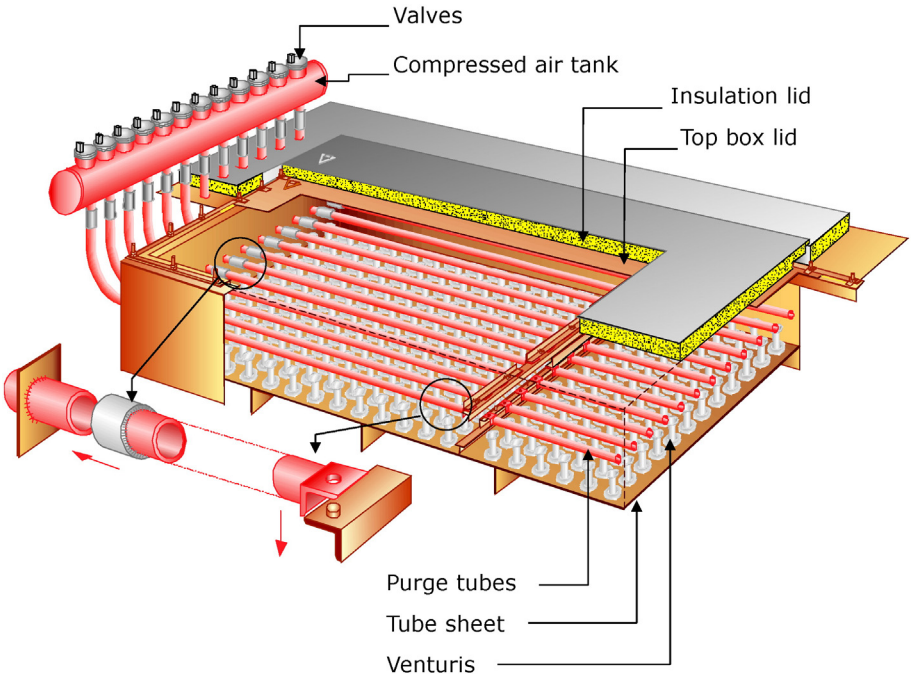

Fig. 1. Schematic view of the pulse-jet cleaning system.

level of detail needed at a fraction of the cost compared to physical experiments.

There are a number of studies in the literature on pulse-jet cleaning, although the majority of the work has focused on high-pressure filters. Previous research has found that several parameters affect pulse-jet cleaning, the most important being: nozzle diameter, distance between nozzle and bag opening, pulse duration, initial tank pressure and volume [1–7]. Bakke [1] identified the jet and venturi concept as essentially a jet pump and found that the pulse pressure developed in the bag is inversely proportional to the flow rate entering the bag. Lu and Tsai [2–4] found that increasing the bag resistance leads to an increase in pulse pressure. Increasing the nozzle diameter was found to increase the pulse pressure until a certain limit, after which a larger diameter will be detrimental; hence an optimum nozzle diameter exists. Similarly, an optimal distance between nozzle exit and bag opening exists. A longer distance allows for more entrainment of secondary air, but if the distance is too long, the jet width will exceed the diameter of the bag or venturi opening. A mathematical model for optimising this distance was later developed by Qian et al. [8], who studied high-pressure filters (6 bar) without venturis.

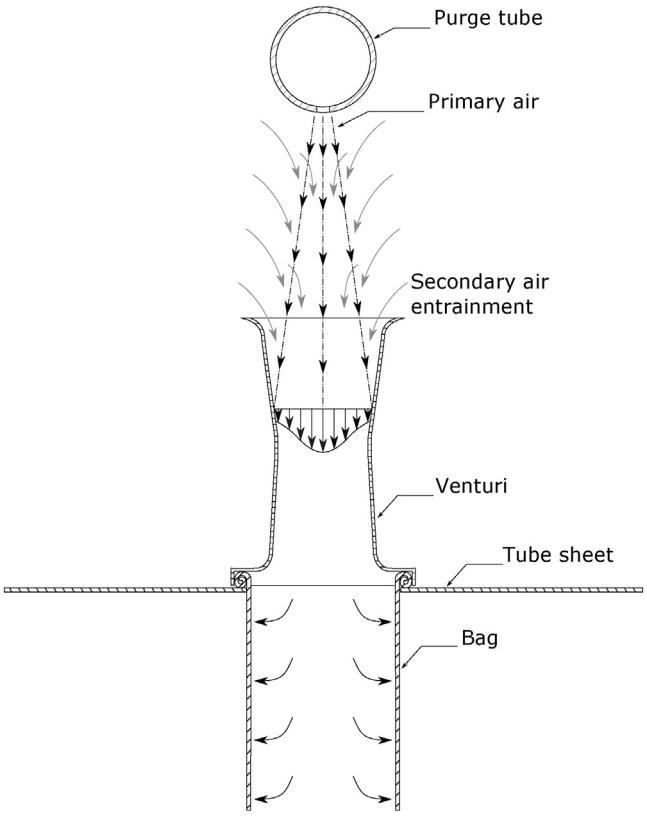

Fig. 2. Illustration of the jet pump principle showing primary air from the nozzle and secondary air entraining the jet from the surroundings.

The role of the venturi is not fully covered in the literature and is a subject of debate. According to Morris et al. [9], the role of the venturi is to allow the pulse to travel easily into the bag, while restricting its escape and thereby increasing the pressure within the bag. The provision of a high pulse pressure was found to be incompatible with a low pressure loss through the venturi during filtration. Removal of the venturi caused significant reduction of the pulse pressure. Lanois and Wiktorsson [10] compared the performance of 'advanced' filters at 1–2 bar tank pressure without venturis to 'traditional' filters at 4.8–6.2 bar with venturis and found that advanced filters require lower energy for the equivalent cleaning efficiency. In the study by Lu and Tsai [4], two venturis were tested against a venturi-less design. The necessity of the venturi was found to depend on the combined resistance of the bag and dust cake. For high resistance bags, maximum pulse pressure was obtained with venturi and vice versa. The venturi role was also studied by Hájek [11], who found a three-fold increase in the mass flow rate entering the bag when installing a venturi, claiming increased entrainment of secondary air to be the reason. Further, a two-fold increase in pulse pressure was found, demonstrating the unambiguous advantage of the venturi. Whether the venturi is beneficial is indeed a subject of debate and is perhaps best summarised by Lu and Tsai [3]: "There are situations where venturis are required to increase pressure pulse inside the bag, and there are also situations where venturis are not necessary."

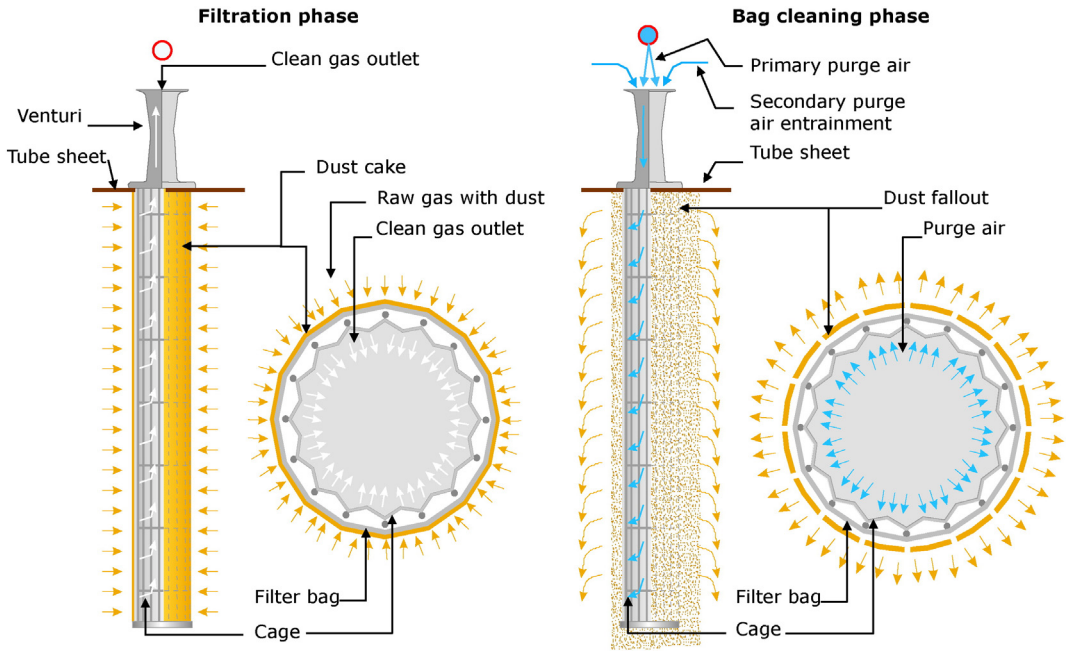

Fig. 3. Schematic view of the bag, steel cage and venturi assembly showing dust cake build-up during normal filtration (left) and dust dislodgement during pulse-jet cleaning (right).

Li et al. [12] studied the effect of installing a cone-shaped structure inside the bag just below the bag opening without the use of venturis. Two different cones were tested against a cone-less design, with both cones leading to an increase in bag pressure as well as peak dust emission during pulse-jet cleaning.

The literature offers only a limited number of CFD-based studies on pulse-jet cleaning. Hájek [11] studied the role of the venturi by using a simplified CFD model consisting of a single bag and straight-bore nozzle with and without venturi. A two-dimensional (2D) mesh was applied, thereby restricting the jet to be axially aligned with the bag, and thus neglecting the possible misalignment between jet and venturi/bag. Unsteady RANS and k-ε turbulence modelling was applied. Lo et al. [7] studied pulse-jet cleaning of a single pleat in a pleated fabric cartridge by CFD. As in the study by Hájek [11], the geometric simplification enforces axial symmetry disregarding the possible axial misalignment between the jet and venturi/bag. Unsteady RANS with the k-ε turbulence model was adopted and isothermal flow assumed despite the non-negligible Mach number and hence the potential cooling due to expansion. Experimental measurements were used as inlet condition at the nozzle and subsequently for validation of the CFD model. Good agreement with experimental results was demonstrated except during pressure ramp-down, this being ascribed to variable filter permeability from fabric deformation, and the assumption of constant uniform filter permeability was questioned. Various CFD models for simulating the filtration flow through pleated filters were assessed by Feng et al. [13]. For high pleat density, LES, DES or v2f RANS was required to predict pressure loss and flow field, whereas for low pleat density the k-ε model performed as well as the more computationally costly models.

The present study concerns CFD and experimental investigation of the pulse-jet cleaning system. Experimental pressure measurements are used as validation data for the full three-dimensional (3D) CFD model, which in turn is used to investigate the basic physics of subsonic/supersonic pulse-jet cleaning, the jet behaviour and the effect of the venturi in relation to a typical pulse-jet cleaned fabric filter. Basic understanding of the physics and the jet and venturi behaviour is essential for optimal cleaning of filter bags, and it remains to be ascertained how these separate parts affect the cleaning system. Detailed results of the full 3D CFD model include jet alignment, pulse pressure inside the bags and the effect of the nozzle and venturi design. For further results based on the present CFD model, the reader is referred to Andersen [14].

2. Methods

2.1. Experimental methods

The experimental pilot-scale test filter is shown in Fig. 4 with specifications listed in Table 1.

The set-up consists of a tank with four internal valves, four purge tubes each with 18 equally spaced straight-bore holes connected by a reinforced rubber connection. For each purge tube, seven holes and bags are placed inside the filter casing making up the test section. The 11 remaining holes in each purge tube are placed outside the casing without bags. Each bag is held in place by an internal steel cage as shown in Fig. 3. The fit between bag and cage is very tight, allowing for less than 5% volume change when the bag is inflated. A venturi device is placed at the opening of each bag, and a tube sheet separates the dust zone from the clean zone. All tests are conducted without dust. Instead, the presence of a dust cake is simulated by using special bags with low permeability, providing exactly the same pressure loss as a conventional bag with dust cake just before cleaning.

Pressure measurements are performed experimentally at seven locations: in the tank and at three positions in each of bag-1 and bag-7 (top, middle and bottom). A pressure transmitter is mounted directly in the tank, whereas 3.5 m long PTFE hoses are used between the measurement location and the transmitter for all six bag measurements.

All tests are performed at room temperature and with the filter in off-line mode, i.e. without filtration flow. Pulse-jet cleaning is performed with an initial tank pressure of 2 bar gauge and 50 ms electrical on time (EOT).

2.2. Numerical methods

The flow during pulse-jet cleaning is characterised as being both supersonic and subsonic. Internally in the purge tube and within the pulse-jet cores, the supersonic flow is dominated by inertial forces, compressibility and the presence of pressure and shock waves. In the pulse-jet shear layer and within the bags, the flow is subsonic and turbulent, whereas the flow is laminar through the filter medium. Since turbulence only plays a role in certain areas, the computationally costly methods for accurately resolving the turbulent scales (e.g. LES, DES) are considered unnecessary. Viscous effects are present in, for example, the

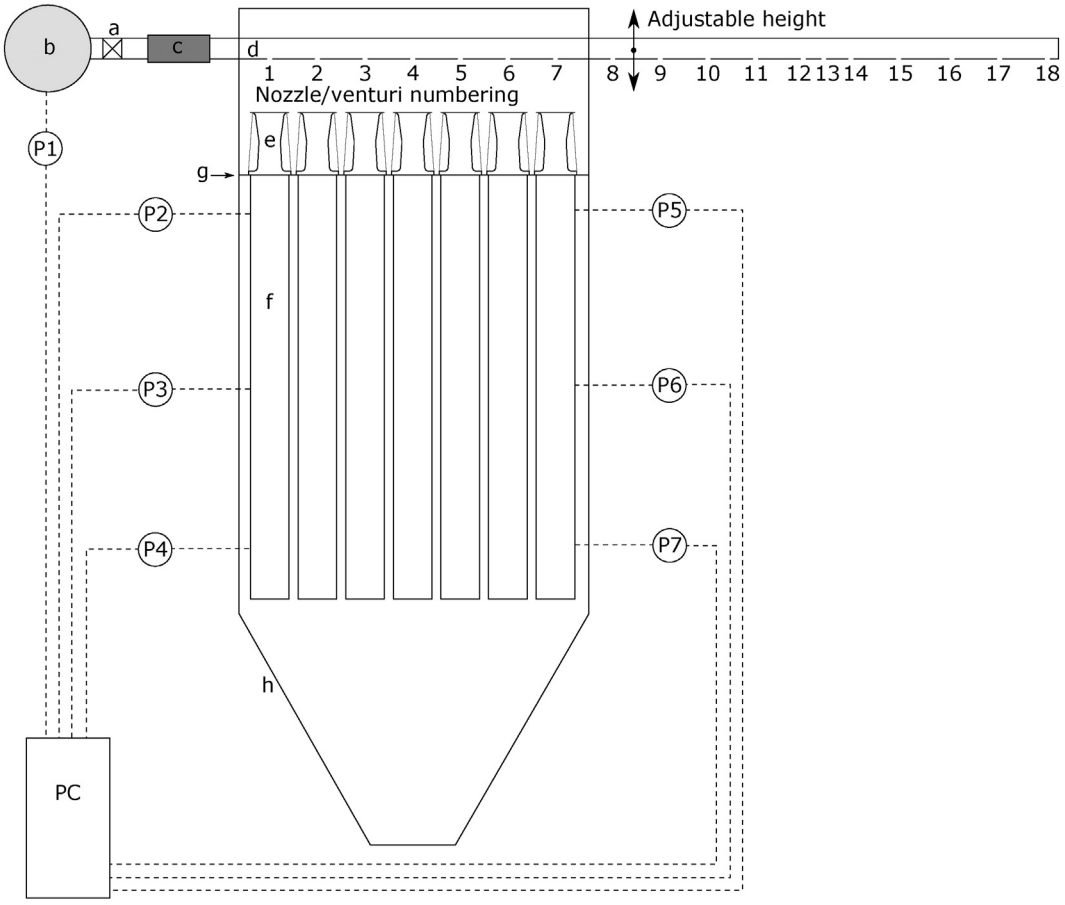

Fig. 4. Schematic illustration of the experimental pilot-scale test filter: (a) valve, (b) compressed air tank, (c) reinforced flexible rubber connecting piece, (d) purge tube with 18 nozzles, (e) venturi, (f) bag, (g) tube sheet, (h) casing, (P1)–(P7) pressure measurement. See Table 1 for full description of components.

pulse-jet shear layer; hence the inviscid assumption often used for supersonic flows cannot be applied. The unsteady RANS formulation (URANS) is therefore considered the optimal compromise. The coupled method of solving the Navier–Stokes (NS) equations, as opposed to the segregated or uncoupled, is suitable for shock waves and highly compressible flows [15,16]. The coupling applies to all three conservation equations as described below.

The commercial code STAR-CCM+ is used to simulate the complex flow in the pulse-jet cleaning system. For detailed information on fluid flow and computational methods, the reader is referred to the STAR-CCM+ user guide [15] and literature, e.g. [16,17].

Table 1
Components of the experimental pilot-scale test filter as illustrated in Fig. 4.

Object		Type
a	Valve	Trimec piston valve 3 in
b	Tank	Volume 225 L
c	Flexible connection	Reinforced rubber
d	Purge tube	18 nozzles, total length ≈3.6 m
e	Venturi	78 mm (throat)
f	Bag	Nomitec polyester weave low permeability, 5 L/dm^2/min @200 Pa, 127 mm ≈ 5 in
g	Tube sheet	Steel plate
h	Casing	Steel plates
Pressure measurement		**Type**
P1	Tank	BD Sensors model DMP 331, 0–10 bar, 4–20 mA
P2	Bag-1, top, 0.5 m below tube sheet	FilTEq GmbH model DS2-420 Platine, −60 to 60 mbar, 4–20 mA
P3	Bag-1, middle, vertical centre of bag	as P2
P4	Bag-1, bottom, 0.5 m above bag bottom	as P2
P5	Bag-7, top, 0.5 m below tube sheet	as P2
P6	Bag-7, middle, vertical centre of bag	as P2
P7	Bag-7, bottom, 0.5 m above bag bottom	as P2

2.2.1. Governing equations

The governing equations are the NS equations including conservation of: mass (continuity), momentum (Newton's second law) and energy (first law of thermodynamics). The conservation of mass is written for compressible fluids in Eq. (1). The Cartesian form and the Einstein notation are used throughout this article.

$$\frac{\partial \rho}{\partial t} + \frac{\partial (\rho u_i)}{\partial x_i} = 0 \tag{1}$$

where ρ is the density, t is the time, u_i is the velocity vector and x_i is the spatial vector [16]. The conservation of momentum, neglecting gravitation, is given by [16]:

$$\frac{\partial (\rho u_i)}{\partial t} + \frac{\partial (\rho u_j u_i)}{\partial x_j} = \frac{\partial \tau_{ij}}{\partial x_j} - \frac{\partial p}{\partial x_i} \tag{2}$$

where τ_{ij} is the viscous and turbulent stress tensor and p is the pressure.

The conservation of energy is given by [17]:

$$\rho\left(\frac{\partial h}{\partial t}+u_i\frac{\partial h}{\partial x_i}\right)=\frac{\partial p}{\partial t}+u_i\frac{\partial p}{\partial x_i}+\frac{\partial}{\partial x_i}\frac{\partial T}{\partial x_i}+\tau_{ij}\frac{\partial u_i}{\partial x_j} \tag{3}$$

where h is the enthalpy, k is the thermal conductivity and T is the temperature. For compressible flows, the density follows from the continuity Eq. (2). The temperature can be computed from the energy Eq. (3). With both density and temperature known, the pressure can be computed from the equation of state where the ideal gas law is applied [17]:

$$p=\rho RT \tag{4}$$

R denoting the gas constant.

2.2.2. Numerical models

Turbulence is modelled by the realisable k-ε model developed by Shih et al. [18] using a second-order upwind convection scheme. The near wall region is treated by the two-layer wall function by Rodi [19]. To account for compressibility, the compressible dissipation dilatational term by Sarkar and Lakshmanan [20] is added to the turbulence transport equation. Due to the mainly sonic nature of the flow, the choice of turbulence model is expected to have only minor influence. The k-ω SST turbulence model by Menter [21] has also been applied (again with compressibility modification); however, no significant change in the result was found and will therefore not be treated further.

Previous numerical studies were limited by axial symmetry, thereby disregarding any possible axial misalignment between jet and venturi/bag [7,11]. In order to simulate the effects of having multiple nozzles in one purge tube and to fully capture the spatially complex flow field in the nozzle and jet, a 3D model is required. Further, experimental validation is of utmost importance, and the geometry of the numerical model must therefore closely resemble the experimental set-up. The computational domain is depicted in Fig. 5 with the different boundary conditions highlighted in colors.

The bags are simulated as having zero thickness with a porous interface applied on the cell faces acting as a membrane allowing fluid to pass whilst experiencing a pressure loss defined by:

$$\Delta p=-\rho\beta v_n \tag{5}$$

where Δp denotes the pressure drop in Pa, ρ is the gas density in kg/m^3, β is the porous viscous resistance in m/s and v_n is the boundary-normal velocity in m/s. This linear expression is suitable during normal operation (filtration) where the flow across the filter is dominated by viscous forces due to the very low velocity $v_n \approx 1$ m/min $= 0.0167$ m/s where

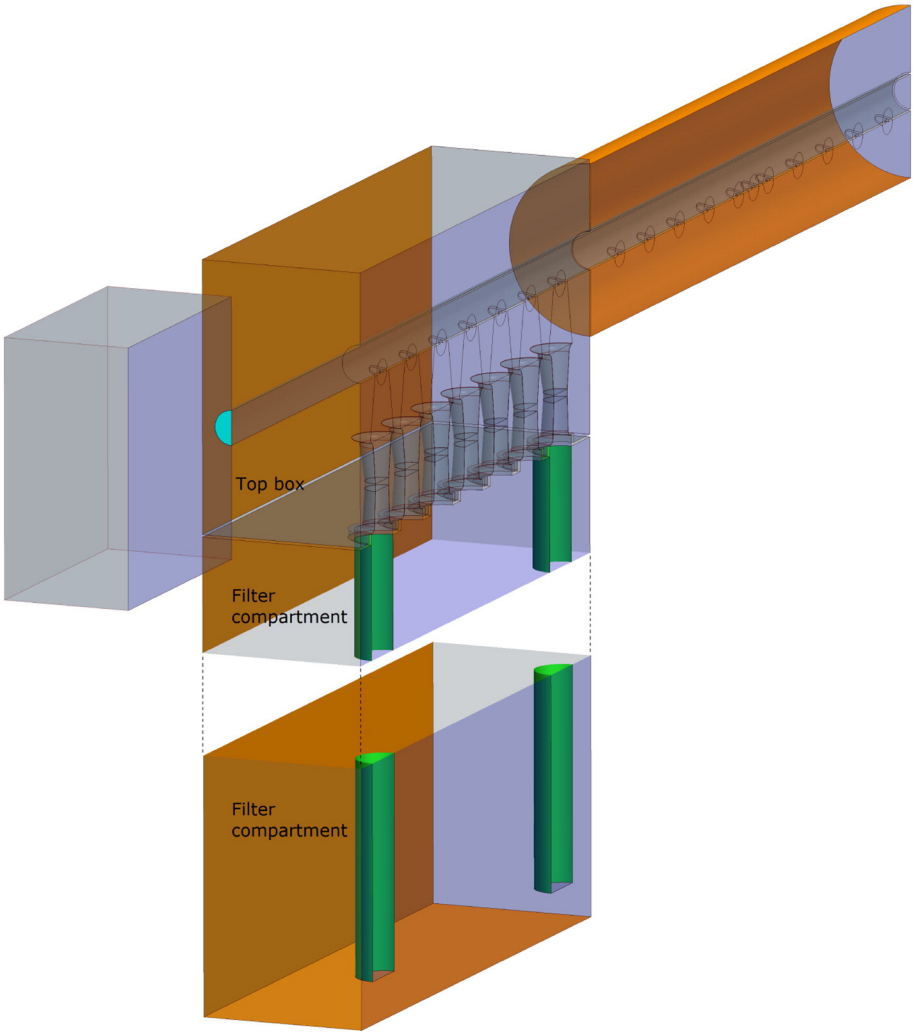

Fig. 5. Computational domain in transparent view. The central part of the filter compartment is omitted for clarity. The boundary types are indicated by colours: orange: outlet, blue: symmetry, green: porous baffle (bag), cyan: porous baffle (valve), grey: wall. (For interpretation of the references to color in this figure legend, the reader is referred to the web version of this article.)

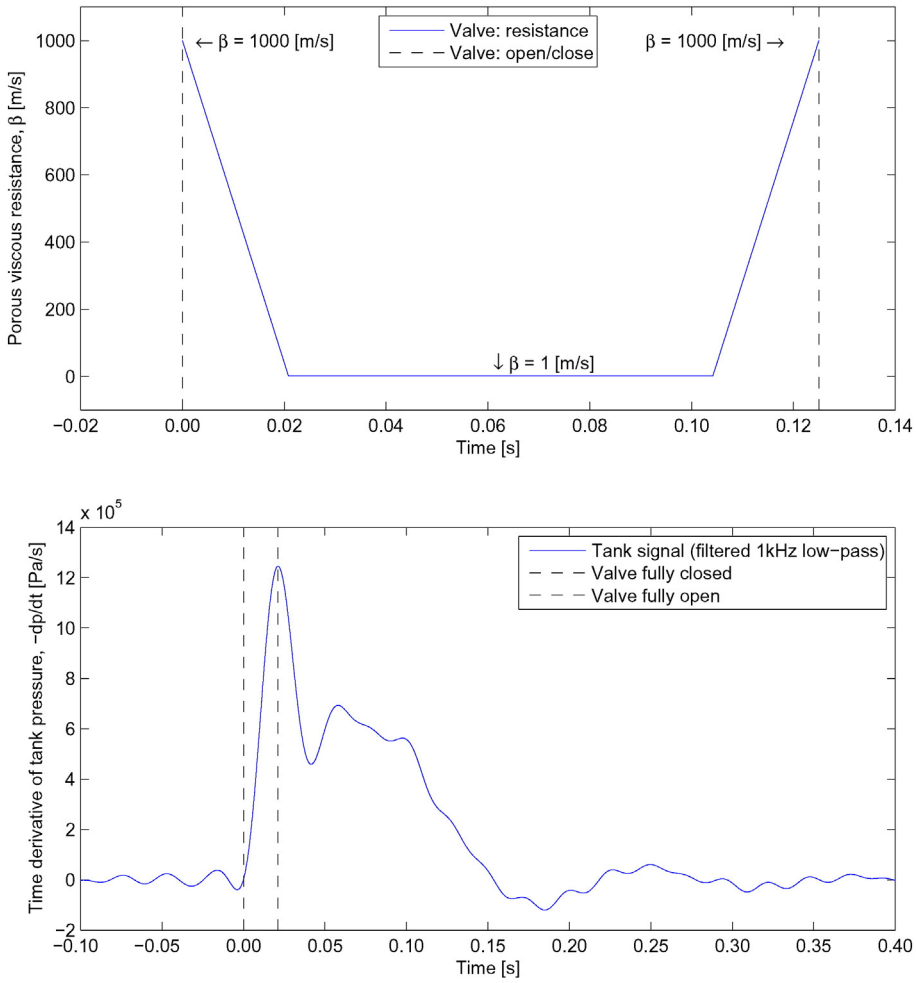

Fig. 6. Upper: input for controlling the valve porous baffle resistance. Figure showing porous viscous resistance, β in Eq. (5), as a function of time. Lower: time derivative of tank pressure (experimental) as a function of time. Used to determine the valve opening time.

the pressure drop across the filter is approximately 1000 Pa. Given the bag peak pressure of 2000–5000 Pa during cleaning, the equivalent increase in v_n (in reverse direction) is considered sufficiently low to still assume viscous dominance. Previous studies show that bag resistance has a major effect on the peak pulse pressure obtained within the bag [1,2,4,7]. Adjusting the value of β to obtain a proper fit with the present experimental data is therefore highly important. For the bags, β is assumed to be constant spatially and temporally. According to Lo et al. [7], the bag resistance varies as the bag is deflected, particularly during the pressure ramp-down, which is of less interest in this study. The bags are modelled as rigid structures neglecting the potential effect of bag deflection. While bag deflection will affect the pulse pressure, the deflection in the pilot-scale test filter is very small (see Section 2.1); hence the assumption is considered valid.

The valve is modelled similarly to the bags, but with temporal variation of the resistance coefficient, β, to represent the characteristics of the

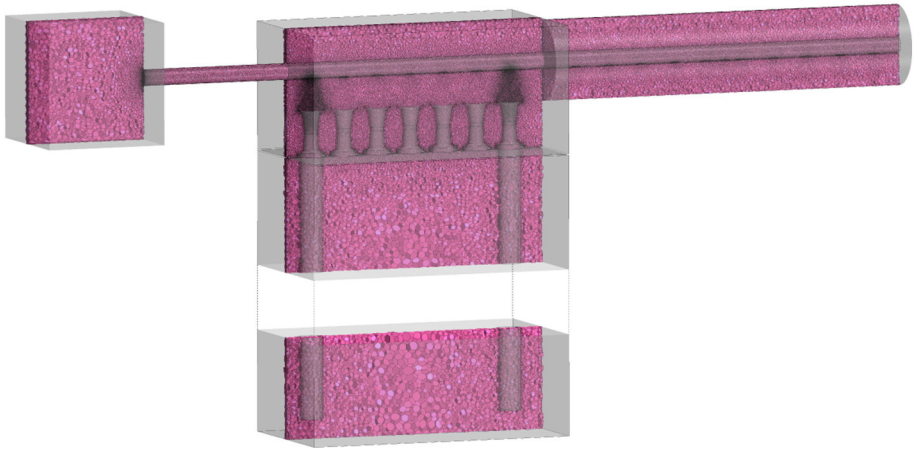

Fig. 7. 3D visualisation of the mesh. For clarity, the geometry is mirrored along the symmetry plane.

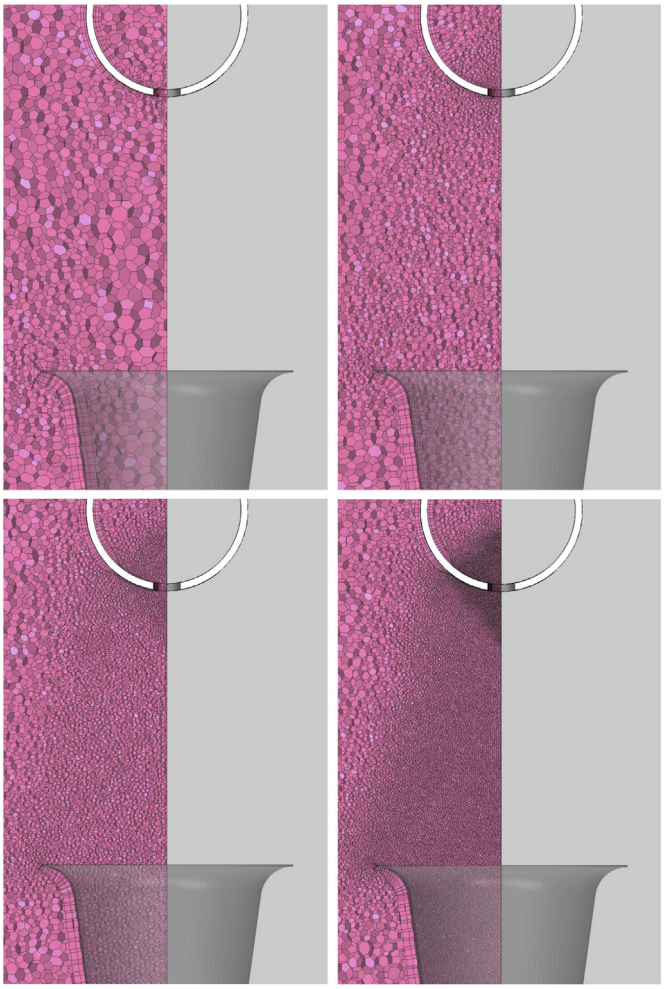

Fig. 8. 3D visualisation of the four mesh levels. Coarse mesh (upper left), Medium mesh (upper right), Fine mesh (lower left), Extra Fine mesh (lower right). View in the axial direction of the purge tube. For clarity, the geometry is mirrored along the symmetry plane.

actual valve. The operation of the valve is simplified by three phases: (1) valve is nearly closed: high resistance; (2) valve is fully open: low resistance but non-zero; and (3) valve returns to closed position: high resistance. The progress between the three phases is approximated by a linear variation of the resistance as illustrated in Fig. 6 with timings determined from the experimental results. Fig. 6 also shows the time derivative of the experimental tank pressure measurement. The transition from zero-gradient to peak-gradient is 21 ms, which corresponds to the time it takes the valve to go from fully closed to fully open. The closing phase is of less interest in this study; hence the same value is applied here. The entire opening time (i.e. phases 1 through 3) is estimated at 125 ms from the experimental tank measurement, leaving 83 ms for the fully opened phase. When the simulation time of 125 ms is reached, the porous interface is converted to a wall hindering any exchange of mass. The simulation is continued until 250 ms. Valve resistance values are determined through trial and error.

2.2.2.1. Spatial and temporal discretisation. The presence of shock waves suggests applying an explicit time-stepping approach. However, as the duration of the pulse-jet is long relative to the jet speed, this will require undesirable small time steps, and the implicit method is adopted instead. Between two time steps, inner iterations are performed based on the default Courant number $C = u\Delta t/\Delta x = 50$, where Δx denotes the grid spacing, which is converted into an inner iteration step size by the software [15].

The inner iterations continue until one of the following two conditions are met: (1) the non-dimensional continuity residual has reached an absolute value of 2×10^{-7} or (2) 15 inner iterations are performed. In essence, the choice of time scheme and settings is a trade-off between numerical accuracy, stability and computational speed. First-order temporal discretisation is used to increase stability when shocks are present [16], although it was found to be quite insensitive to modifications of solver settings (including time step and inner iteration Courant number).

The computational domain is composed of unstructured polyhedral cells with sizes specified in certain regions. High spatial resolution is applied to regions where large gradients are found as shown in Fig. 7. Four meshes with varying spatial resolution are constructed as shown in Fig. 8. Properties and computational times for the four meshes are listed in Table 4. A constant time-step size of $\Delta t = 1 \times 10^{-5}$ s is used, resulting in different maximum convective Courant numbers for the four meshes.

The shock front speed was found to be independent of the mesh resolution; hence no refinement is applied internally in the purge tube and bags. However, the flow field in the jet and nozzle, including the near-field region, was found to be mesh sensitive, due to the larger gradients present there. The Coarse mesh strongly overpredicts the width of the jet which affects the flow in the venturi and ultimately the pulse pressure. The Extra Fine mesh provides an overly resolved jet and very good agreement with experimental results. Based on the quality of the results compared to the computational effort, the Fine mesh is chosen for the majority of the further analyses.

2.2.2.2. Boundary conditions. Pressure outlets with a total pressure equal to 0 Pa (relative to the reference pressure) are applied in the top box and filter compartment to simulate an infinitely large volume on both sides of the tube sheet. During pulse-jet cleaning, entrainment of secondary air from the top box plenum causes a pressure reduction of the enclosed volume in the top box and an increase in filter compartment pressure as also indicated by Hájek [11]. For small filters, this will greatly influence

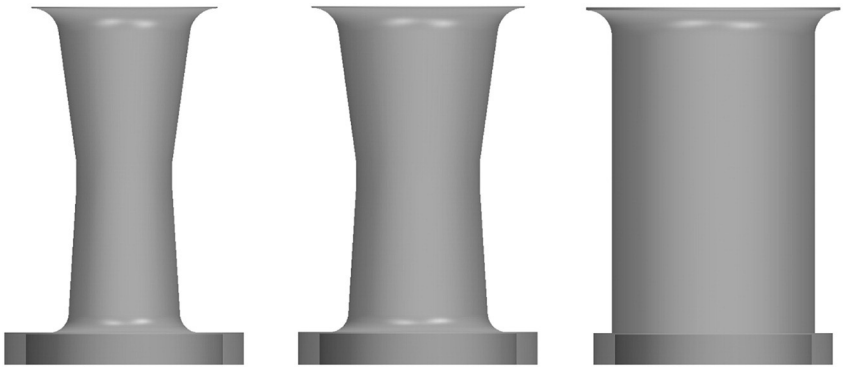

Fig. 9. Geometry of the three venturi configurations. From left to right: small venturi (throat 60 mm), large venturi (throat 78 mm) and no venturi (127 mm).

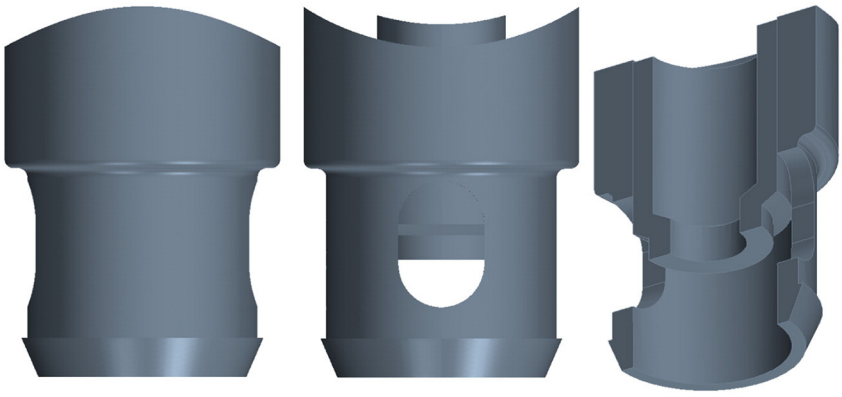

Fig. 10. Add-on nozzle geometry.

the pulse pressure, but for larger filters and when including the volume of adjoining ducts, the effective volume is large and the approximation of infinite volume thus becomes realistic. Inflow may occur on the pressure outlet boundaries in which case a temperature of 300 K is applied.

A symmetry boundary condition is applied along the vertical plane through the centreline of the bags and purge tube. This approximation is suitable during the majority of the time domain, where the high velocity flow is dominated by inertial forces and the jet is highly stable. The possible asymmetry during jet build-up/decay is not considered.

The wall type boundary condition with the no-slip condition is applied to the remaining surfaces as indicated in grey in Fig. 5. Wall boundaries are assumed adiabatic.

2.2.2.3. Initial conditions. The computational domain is initialised by applying a pressure of 2 bar to the tank volume and 0 bar to the remaining parts of the domain, both relative to the reference pressure of 1.01325 bar. A temperature of 300 K is applied throughout the domain. Bidirectional pressure waves will emanate from the valve from the beginning of the simulation ($t=0$) due to the porosity having a finite value.

The tank volume is widely known to influence the pulse pressure obtained within the bags [2–4,6,7,22] and is therefore adjusted accordingly to 225 L in the numerical model taking symmetry into account. The shape and tank internals are assumed insignificant; for simplicity, a square box is used.

2.2.3. Model applications

Following the validation by experimental pressure data, the numerical model is modified to study different applications, including venturi and nozzle design. The venturi is known to influence the pulse pressure obtained within the bag as well as the pressure loss across the venturi during filtration [1,3,4,9,11,22–24]. Three configurations of the numerical model are built to study the flow field and pressure dependency upon the venturi. A configuration essentially without venturi and two variations of the venturi throat diameter are studied (Fig. 9).

The baseline geometry features a simple straight-bore nozzle suspected to cause misalignment between jet and venturi due to the flow direction in the purge tube and the relatively small wall thickness. A commercially available add-on nozzle (Fig. 10) claiming to improve alignment is studied in comparison to the simple nozzle.

3. Results and discussion

3.1. Pulse-jet flow characteristics

The flow field in a pulse-jet cleaning system is inherently different from traditional jet theory. The latter is beyond the scope of the present study. Several factors complicate the flow field, the most important being: strong compressible effects, highly transient behaviour, imperfect nozzle design and non-uniform upstream flow conditions. For simplicity, the jet characteristics are divided into two phases:

1. The *subsonic phase* during jet ramp-up is dominated by large instabilities, the formation of a vortex ring and strong dynamic fluctuations (Figs. 11 and 12).
2. The *supersonic phase* is quasi-steady with velocities exceeding the local speed of sound (Fig. 13).

After the supersonic phase, the jet returns to the subsonic phase during ramp-down, although without the formation of a vortex ring.

A compressible vortex ring structure (Fig. 11) is formed in the shear layer between the jet and the surrounding stagnant air during the subsonic jet build-up when the jet momentum is relatively low and the jet is subject to a Kelvin–Helmholtz-like instability. This is consistent with

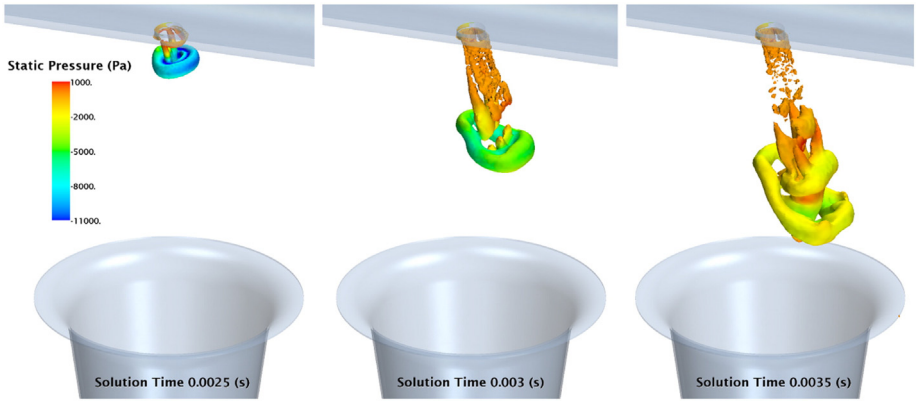

Fig. 11. Formation of a compressible vortex ring structure during the subsonic phase of the jet visualised by an isosurface of the λ_2 criterion with isovalue $=-1\times10^{-7}$. For definition of the λ_2 criterion, see Chakraborty et al. [32]. Results obtained with the Extra Fine mesh.

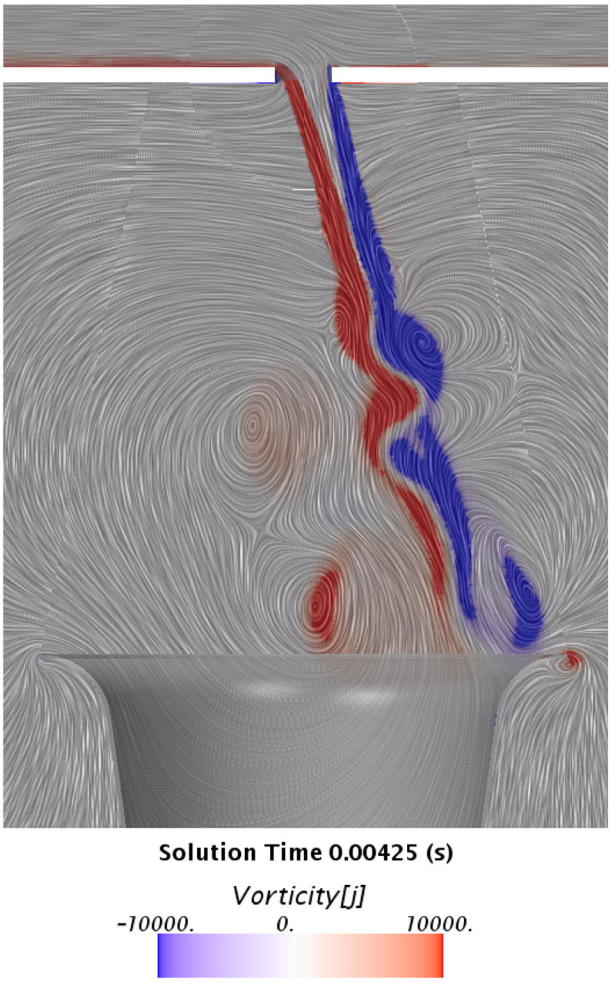

Fig. 12. Vorticity in the y-direction (out-of-plane) and vector field showing the dynamically oscillating jet in the subsonic phase. Results obtained with the Extra Fine mesh.

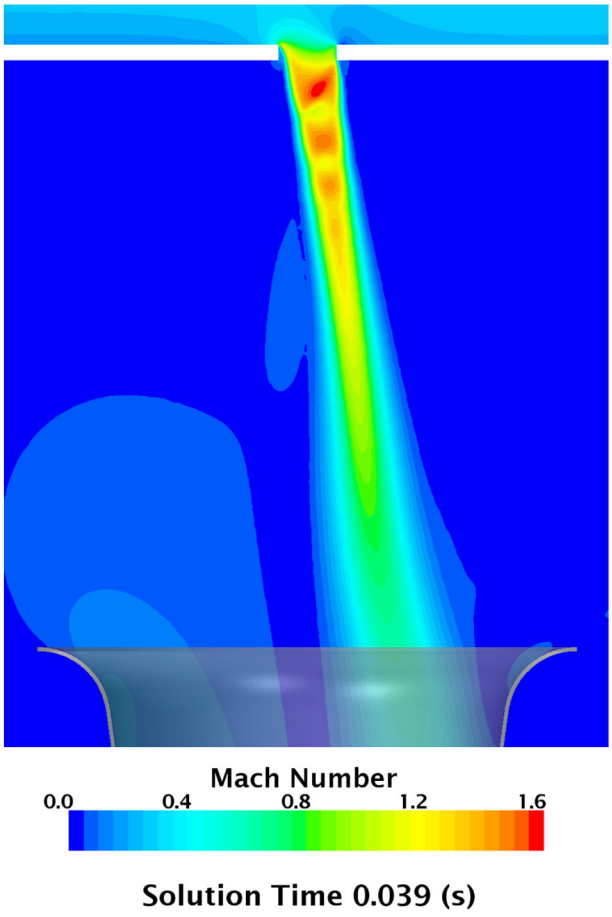

Fig. 13. Shock cells visualised by the local Mach number in the jet when at its maximum speed. Results obtained with the Extra Fine mesh.

the findings by Lim [25] and Murugan et al. [26]. Subsequently, more vortex rings are formed, but due to the rapid breakdown, these are less visible and not well-defined. The instabilities cause the jet to fluctuate dynamically (Fig. 12).

The vortex rings and instabilities occur only in the subsonic phase, when the jet momentum is low. In the supersonic phase, the jet velocity exceeds the sonic limit locally and, depending on the spatial discretisation, a characteristic flow pattern occurs. This is visualised in Fig. 13 showing the local Mach number when the jet is at its maximum speed. The phenomenon also known as shock cells or shock diamonds is the result of interaction between shocks within the supersonic jet due to the jet being overexpanded. This causes strong fluctuations of the velocity, temperature, pressure and density within the jet core, which decrease in strength further from the nozzle as the jet is compressed and eventually reaches ambient pressure. The pattern is similar to the findings by Ooi et al. [27] and Panda and Seasholtz [28], but differs due to the fact that this jet is not aligned axially with the nozzle. Accurate simulation of shock cells requires the use of extremely fine spatial discretisation, and the Extra Fine mesh has been applied here for illustrative purpose.

3.2. Validation by pressure measurements

The numerical model is validated by comparison of numerical results and experimental pressure data from the tank and bag-1 (Fig. 14) and bag-7 (Fig. 15) as a function of time. For the tank pressure (Fig. 14), good agreement between numerical and experimental results is seen as a result of the valve control scheme applied (Fig. 6), though the simulation tends to slightly overpredict the emptying of the tank. When the valve opens at $t = 0$ s, the tank pressure decreases rapidly until around $t = 0.04$ s. This is a result of the shock wave propagating through the purge tube and being reflected multiple times until the tank and purge tube pressure approach each other. From $t = 0.05$ s, emptying of the tank takes place at an almost constant rate limited by the pressure difference across the valve and nozzles.

In bag-1 and bag-7, the agreement between numerical and experimental results are found to be satisfactory (Figs. 14 and 15). At the top location, a very high pulse pressure of 3800 Pa is reached within a short time in both bag-1 and bag-7, though the simulation tends to be most accurate in bag-7, top, rather than bag-1, top. Wiggles found during the pressure ramp-up in bag-1, top, are the result of several factors, including the valve resistance control scheme (Fig. 6) and pressure wave reflections within the purge tube. Even if present in the experiment, these are not visible in the experimental data due to the 3.5 m measurement hoses, which dampen such rapid fluctuations.

The top and bottom locations in bag-1 and bag-7 all exhibit distinct periodic oscillations. The complex frequency patterns are the result of oscillation induced into the bag from multiple sources, including: (1) the pulse-jet pressure wave travelling down through the bag at the local speed of sound and being reflected at the bottom by the steel plate, and (2) strong fluctuations in the pulse-jet velocity caused by pressure and shock waves present within the purge tube. This means that several frequencies are present in the bag. E.g. in bag-1, top (Fig. 14), the period of 0.054 s (18.6 Hz) and the total travel length of 2×9.5 m fit well with the speed of sound at room temperature. The

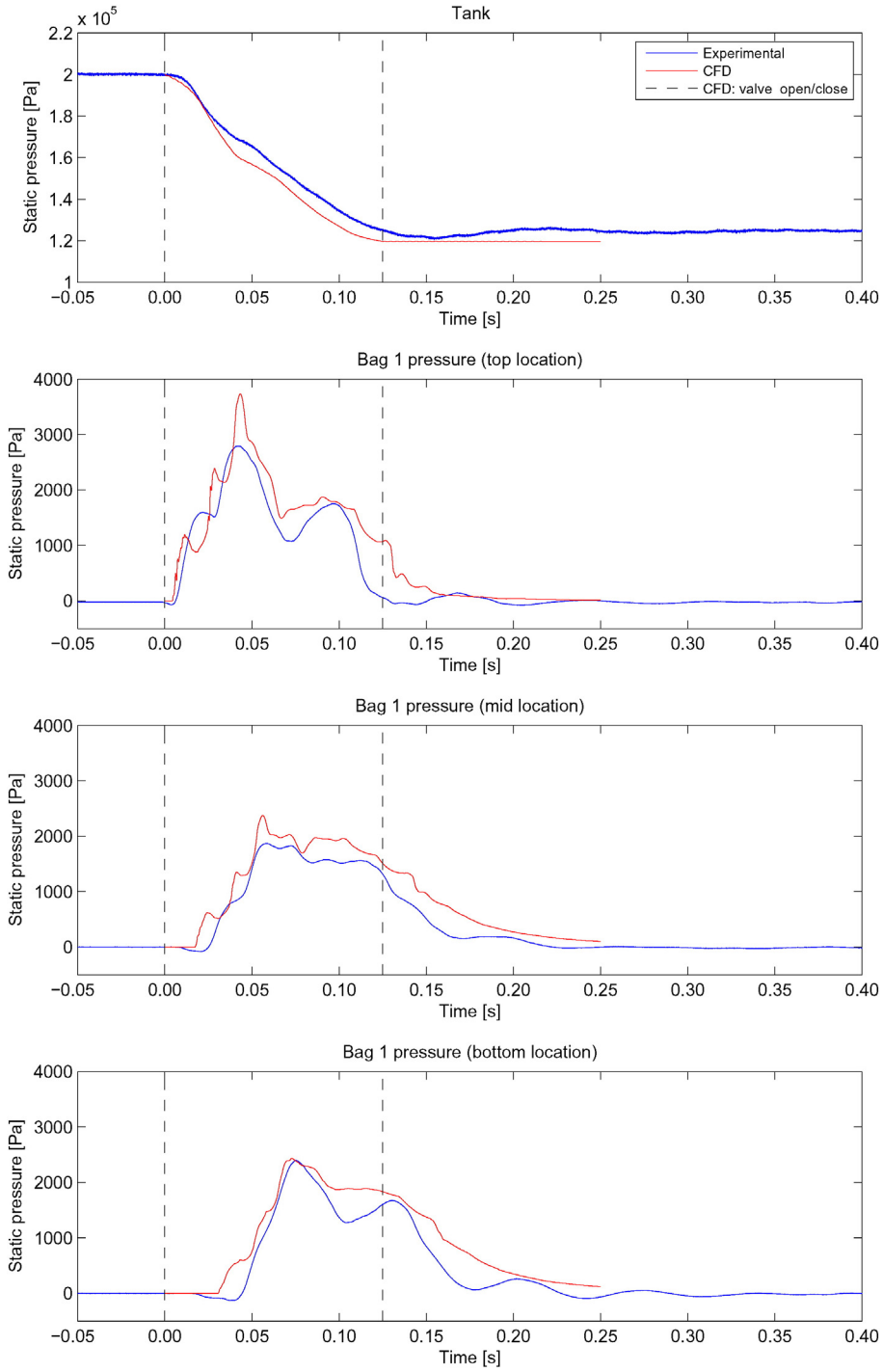

Fig. 14. Static pressure as a function of time in tank and bag-1 showing experimental and CFD results. The Fine mesh and $\beta_{bag} = 35{,}000$ m/s are used.

periodic oscillation is also found at the bottom location, but with a phase shift of 0.032 s. At the middle location of both bags, this periodic oscillation is less visible. The lack of strong periodicity might be caused by wave cancellation and the fact that multiple frequencies are present in the bag.

The peak pressure drops with the axial distance as the pressure wave travels axially downwards through the bag and part of the pulse travels outwards through the bag. This is consistent with the findings by Lim [2] and Murugan et al. [5]. At the middle location, the peak pressure reaches only ≈2000–2300 Pa, which is still sufficient for bag cleaning. According to Löffler [24], 400–500 Pa is needed for good bag cleaning.

At the bottom location, the peak pressure increases to a level slightly lower than at the top location as the pressure wave is reflected in the bag bottom where a steel plate is mounted. This is contrary to the findings by Lu and Tsai [2] and Yan et al. [5]. The discrepancy is ascribed to the steel plate, the high-resistance bag material used in the present study and the fact that no dust is removed; hence the bag resistance remains high throughout the duration of the cleaning.

During the pressure ramp-down (after $t = 0.125$ s), the numerical model overpredicts the pressure in the bags at all locations. This was also found by Lo et al. [7], who ascribed the discrepancy to a variable bag resistance due to, e.g., deformation of the fibre structures within the filter medium upon being inflated. Lo et al. [7] suggest that the

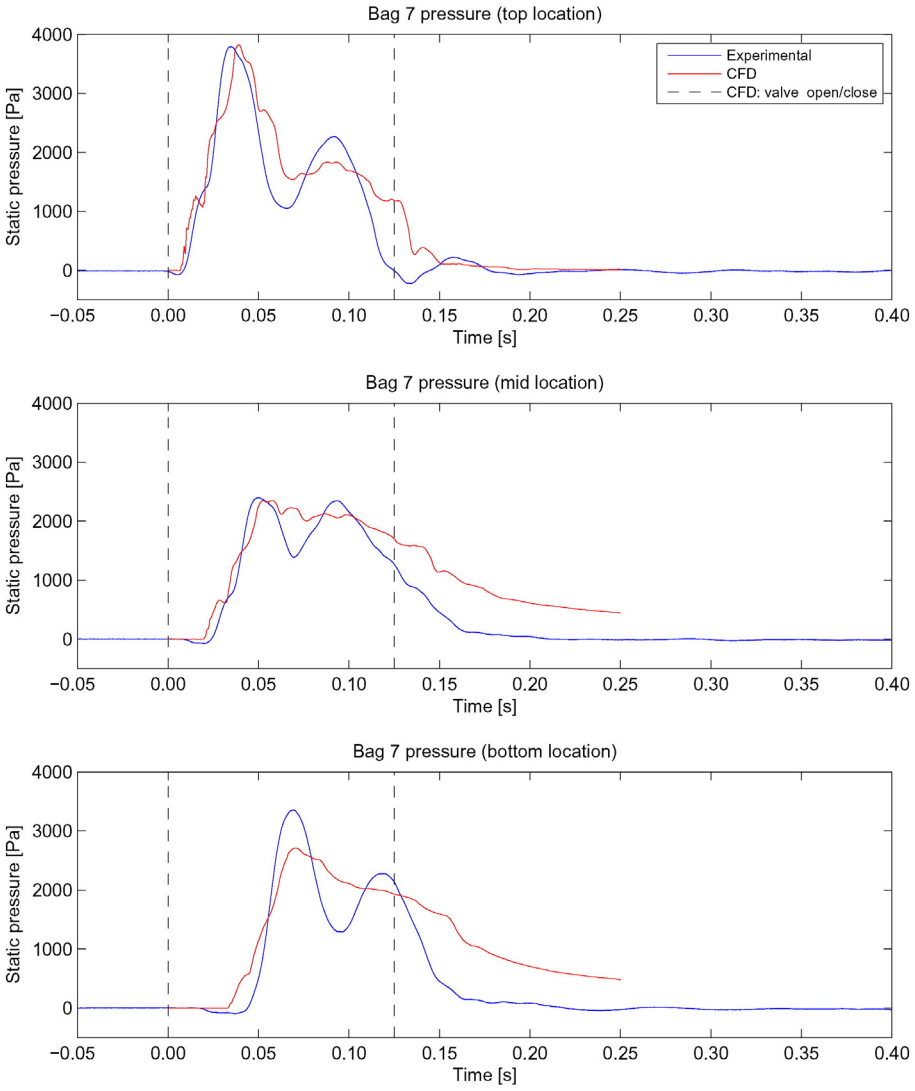

Fig. 15. Static pressure as a function of time in bag-7 showing experimental and CFD results. The Fine mesh and $\beta_{bag} = 35{,}000$ m/s are used.

constant resistance coefficient is a poor assumption, which is fully consistent with the findings of the present study. Accurate modelling of the bag resistance by applying variable coefficients is required to obtain a better match. This is, however, not considered in the present study. Despite some deviation during pressure ramp-down, the agreement between CFD and experimental results is generally good, and the model is considered validated.

3.3. Nozzle type

The two nozzle types mentioned in Section 2.2.3 are tested numerically and compared in Fig. 16 showing the velocity vector field and magnitude in nozzle 1. Three time steps are shown: $t = 0.020$ s when the misalignment is most pronounced, $t = 0.039$ s at the maximum jet speed and $t = 0.050$ s when the alignment is best.

The straight-bore nozzle is found to cause misalignment between the jet and venturi at the nozzles near the tank (see also Fig. 13, Section 3.1), whereas the nozzles far from the tank provide good alignment. This is caused by a reduction in the mass flow rate and hence velocity along the length of the purge tube due to the flow out of the nozzles. In the following, nozzle 1 is of main interest due to the strong misalignment.

During the filling of the purge tube ($t = 0.020$ s), the jet impinges on the edge of the venturi entrance. Upon filling ($t = 0.039$ s), the misalignment is reduced but the jet core is located in the outermost quarter of the venturi throat and remains there throughout the duration of the pulse-jet. This reduces the jet momentum in the axial direction of the bag and, most critically, allows for a backflow zone occupying up to half of the throat area.

For the add-on nozzle, the ability to realign the jet is limited. At $t = 0.020$ s, the magnitude of the misalignment is comparable to the straight-bore nozzle, but the direction has changed towards the opposite side of the venturi. This is due to the non-optimal internal geometry of the add-on nozzle causing a large separation zone before the nozzle exit. At $t = 0.039$ s, the misalignment has improved slightly compared to the straight-bore nozzle. At $t = 0.050$ s, the jet is well aligned, and the jet width fills the venturi throat and thereby eliminates backflow.

To quantify the effect of adding the nozzle, the results of the peak pressure are listed in Table 2. An overall peak pressure improvement of 6–17% by installing the add-on nozzle is seen, with the biggest improvement at the middle and bottom locations where the peak pressure is lowest. The mass flow rate into the bag and the overall pressure level after the peak pressure are increased even further (not shown) by the add-on nozzle. The cleaning mechanism is not fully understood, but several authors point towards peak pressure and mass flow rate being good indicators of cleaning effectiveness [3,8,24,29–31]. The 6–17% peak pressure increase and the even bigger increase in the mass flow rate are likely to cause improved cleaning, given that the bag is not

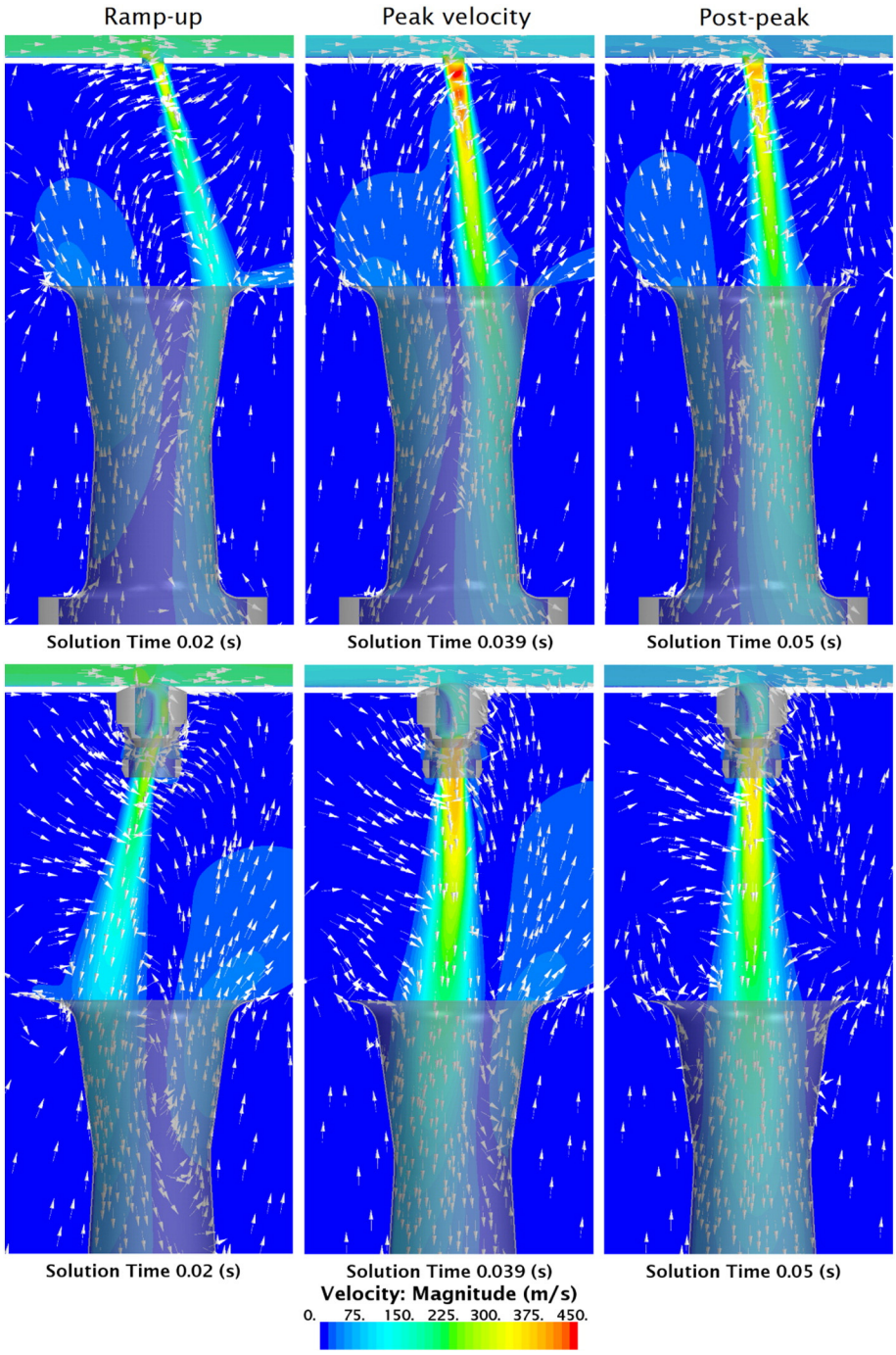

Fig. 16. Velocity vector field and magnitude at nozzle 1. Time progressing from left to right. Upper figures: straight-bore nozzle; lower figures: add-on nozzle.

completely cleaned by the straight-bore nozzle. Further, the peak pressure increase makes it possible to reduce the tank pressure and/or compressed air consumption whilst maintaining sufficient cleaning intensity. Despite having equal diameters, the add-on nozzle was found also to increase the consumption of compressed air by 7% in each pulse, which reduces the saving potential offered by this nozzle although the correlation is not linear. The increased consumption is ascribed to the lower resistance offered by the add-on nozzle geometry (Fig. 10) compared to the straight-bore nozzle.

Table 2
Nozzle comparison based on bag-1 peak pressure.

	Straight-bore Nozzle [kPa]	Add-on Nozzle [kPa]	Increase [%]
Top	3.74	3.96	6
Middle	2.38	2.60	10
Bottom	2.44	2.84	17

3.4. Venturi type

The effect of the venturi is analysed by studying the gas velocity in the axial direction through venturi-1 (Fig. 17), the net mass flow rate entering bag-1 (Fig. 18) and the peak pressure in bag-1 (Table 3) for the three different venturis mentioned in Section 2.2.3 (Fig. 9). Fig. 17 shows that the venturi throat diameter has a direct effect on the gas flow entering and exiting the bag and thus also on the bag cleaning.

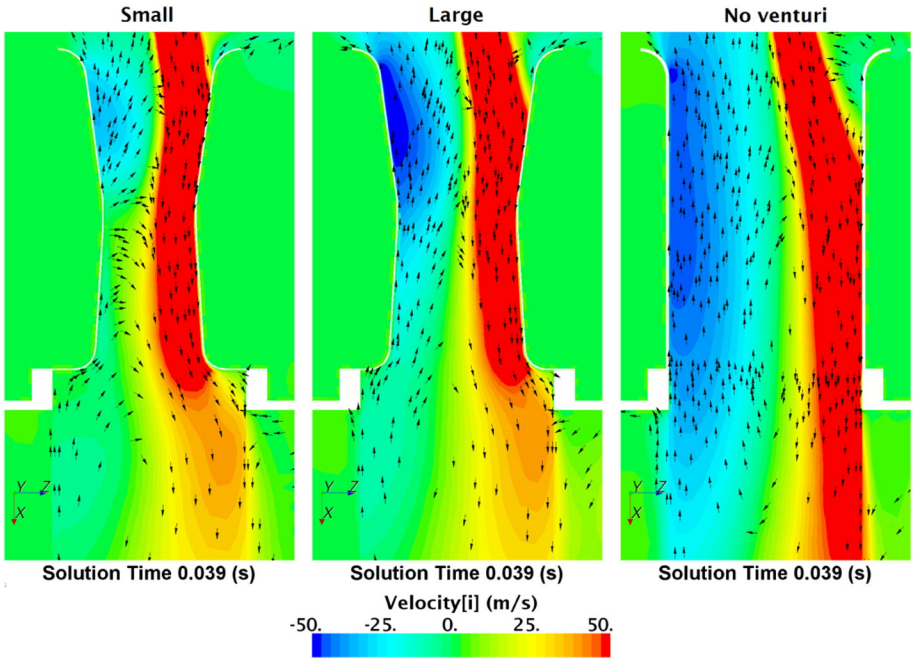

Fig. 17. Axial velocity and velocity vector field for the three venturi configurations. From left to right: small venturi (throat 60 mm), large venturi (throat 78 mm) and no venturi (127 mm). Note: Clipping is disabled and some values exceed the velocity scale bar.

For the large venturi (78 mm), the combination of a large throat and misaligned jet allows for substantial backflow exiting the venturi.

Decreasing the throat diameter (60 mm) is found to reduce the backflow zone (Fig. 17) and increase the net mass flow rate entering bag-1 (Fig. 18). Consequently, the peak pressure is increased by 7–9%, which is a modest improvement.

Removing the venturi (127 mm) allows for significantly increased backflow and reduced net mass flow entering the bag. Consequently, a significant reduction of the peak pressure by 30–34% is seen.

In conclusion, the working principle of the venturi is to restrict backflow which is detrimental to the pulse pressure obtained in the bag. These findings are consistent with [9], who state that the role of the venturi is to allow the pulse to travel easily into the bag, while restricting its escape and thereby increasing the pulse pressure. Both Morris et al. [9] and Lu and Tsai [4] found that decreasing the venturi throat diameter increases the pulse pressure, which is also the conclusion in the present study. Hájek [11] quantified the effect of adding a venturi and found a factor 2 peak pressure increase. Again, this complies with the findings in the present study, although the improvement by adding the small or large venturi is less than a factor 2. The small difference between the small and large venturi points towards both venturi designs being close to a possible optimal throat diameter.

To evaluate the suitability of a venturi design, the pressure loss during filter operation must be taken into account. Ultimately, the choice should be based on a cost optimisation by estimating the power consumption required for cleaning and filter operation, respectively.

4. Conclusions

The flow in a pulse-jet cleaned fabric filter has been investigated numerically using the commercial CFD code STAR-CCM+. A full 3D CFD model simulating the transient pulse-jet cleaning has been developed and validated by experimental pressure measurements. The validated CFD model has been used to investigate the basic physics of low-pressure pulse-jet cleaning (2 bar), jet misalignment and the effect of venturi and nozzle design.

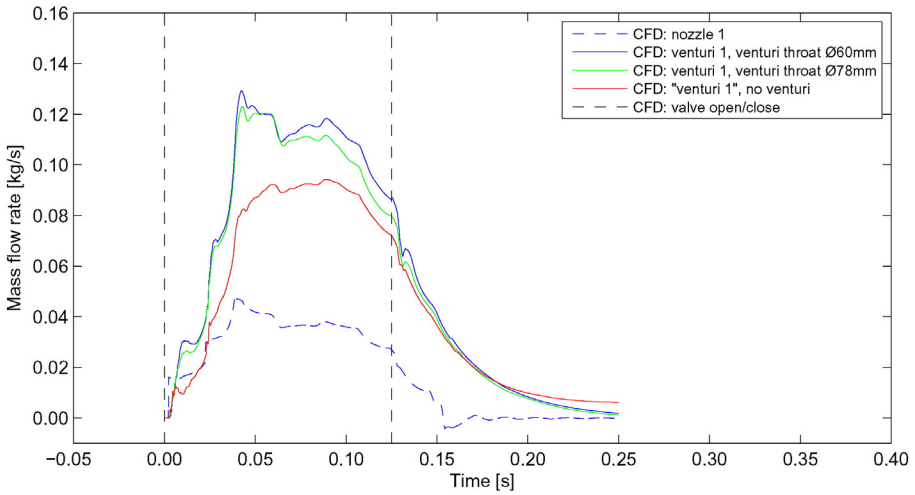

Fig. 18. Mass flow rate through nozzle and venturi-1 as a function of time for the three venturi configurations.

Table 3
Venturi comparison based on bag-1 peak pressure.

Venturi	Large	Small	Increase	No venturi	Increase
	[kPa]	[kPa]	[%]	[kPa]	[%]
Top	3.74	4.06	9	2.45	−34
Middle	2.38	2.58	8	1.64	−31
Bottom	2.44	2.61	7	1.71	−30

Experimental measurements of the tank pressure and pulse pressure within two bags in a pilot-scale test filter were recorded during pulse-jet cleaning and used for validation of the CFD model. Good agreement between experimental and CFD measurements in the tank was found as a result of the valve being modelled as a porous interface with resistance varying in time. Key features such as the pulse pressure ramp-up, peak and oscillations within the two bags were captured well by the CFD model, showing good agreement with experimental measurements. The CFD model was found to overpredict the pulse pressure during pressure ramp-down. Despite this deviation, the agreement between CFD and experiment was generally good, and the model is considered validated.

The pulse-jet was found to show highly transient behaviour whilst cleaning. During the subsonic ramp-up of the jet, large instabilities were observed in the shear layer between the jet and the surrounding stagnant air, leading to the formation of several compressible vortex rings. Subsequently, the jet became supersonic, clearly showing shock cells in the overexpanded jet.

The effect of the nozzle design was investigated by testing a straight-bore nozzle typical for fabric filters and an add-on nozzle with equal exit diameter. The straight-bore nozzle was found to cause substantial misalignment between the pulse-jet and the bag at the nozzles near the tank. This was due to the high axial velocity in the purge tube and the relatively low wall thickness, which is most pronounced for low-pressure filters. Axial velocity in the purge tube, and therefore misalignment, decreased along the length of the purge tube due to the flow out of the nozzles. An add-on nozzle designed to correct this showed limited ability to realign the jet due to the non-optimal internal design of the add-on nozzle. The pulse pressure within the bag was increased by 6–17% at the cost, however, of a 7% increase in compressed air consumption.

The role of the venturi was investigated by studying the gas velocity through the venturi, the net mass flow rate into the bag and the peak pulse pressure in the bag for three designs: a small throat venturi (60 mm), a large throat venturi (78 mm) and no venturi. A large venturi throat diameter allowed for substantial backflow exiting the venturi, particularly in combination with the misaligned jet. Reducing the venturi diameter restricted the flow from escaping the bag, thereby increasing the peak pulse pressure by 7–9%. Removal of the venturi allowed for a significant increase in backflow, a reduced mass flow rate into the bag and a 30–34% reduction in the peak pulse pressure. In conclusion, the working principle of the venturi is to restrict the flow from escaping the bag and thereby maximise the mass flow and peak pressure in the bag.

In summary, the present work highlights the importance of understanding the complex physics of pulse-jet cleaning and the challenges introduced by low-pressure cleaning. The present 3D CFD model has been validated by experimental pressure measurements and is capable of capturing details in the flow not previously seen. It has been shown that 3D unsteady RANS simulation is suitable for optimising the pulse-jet cleaning system design in fabric filters.

Table 4
Number of cells, maximum convective Courant number and computation time on a 16-core Sandy Bridge HPC node. *NB: refinement at nozzle/jet 7 is disabled for the Extra Fine mesh to limit the cell count.

Mesh	Coarse	Medium	Fine	Extra Fine
Number of cells	591,484	650,453	920,635	1,441,787*
Courant number	1.7	3.5	7	14
Computation time [h]	23	25	33	56

References

[1] E. Bakke, Optimizing filtration parameters, J. Air Pollut. Control Assess. 24 (12) (1974) 1150–1154, http://dx.doi.org/10.1080/00022470.1974.10470027.
[2] H.C. Lu, C.J. Tsai, Numerical and experimental study of cleaning process of a pulse-jet fabric filtration system, Environ. Sci. Technol. 30 (11) (1996) 3243–3249, http://dx.doi.org/10.1021/es960020u.
[3] H.C. Lu, C.J. Tsai, A pilot-scale study of the design and operation parameters of a pulse-jet baghouse, Aerosol Sci. Technol. 29 (6) (1998) 510–524, http://dx.doi.org/10.1080/02786829808965587.
[4] H. Lu, C. Tsai, Influence of design and operation parameters on bag-cleaning performance of pulse-jet baghouse, J. Environ. Eng. 125 (6) (1999) 583–591, http://dx.doi.org/10.1061/(ASCE)0733-9372(1999)125:6(583).
[5] C. Yan, G. Liu, H. Chen, Effect of induced airflow on the surface static pressure of pleated fabric filter cartridges during pulse jet cleaning, Powder Technol. 249 (2013) 424–430, http://dx.doi.org/10.1016/j.powtec.2013.09.017.
[6] L.M. Lo, D.R. Chen, D.Y. Pui, Experimental study of pleated fabric cartridges in a pulse-jet cleaned dust collector, Powder Technol. 197 (3) (2010) 141–149, http://dx.doi.org/10.1016/j.powtec.2009.09.007.
[7] L.M. Lo, S.C. Hu, D.R. Chen, D.Y. Pui, Numerical study of pleated fabric cartridges during pulse-jet cleaning, Powder Technol. 198 (1) (2010) 75–81, http://dx.doi.org/10.1016/j.powtec.2009.10.017.
[8] Y. Qian, Y. Bi, Q. Zhang, H. Chen, The optimized relationship between jet distance and nozzle diameter of a pulse-jet cartridge filter, Powder Technol. 266 (2014) 191–195, http://dx.doi.org/10.1016/j.powtec.2014.06.004.
[9] K. Morris, C. Cursley, R.W.K. Allen, The role of venturis in pulse-jet filters, Filtr. Sep. 28 (1) (1991) 33–36, http://dx.doi.org/10.1016/0015-1882(91)80039-8.
[10] G. Lanois, A. Wiktorsson, Current status and future potential for high-ratio fabric filter technology applied to utility coal-fired boilers, Proceedings of the 1st Conference on Fabric Filter Technology for Coal-Fired Power Plants, 1982.
[11] J. Hájek, Computational fluid dynamic simulations in thermal waste treatment technology — design, optimisation and troubleshooting, Energy 33 (6) (2008) 930–941, http://dx.doi.org/10.1016/j.energy.2007.11.010.
[12] J. Li, S. Li, F. Zhou, Effect of cone installation in a pleated filter cartridge during pulse-jet cleaning, Powder Technol. 284 (2015) 245–252, http://dx.doi.org/10.1016/j.powtec.2015.06.071.
[13] Z. Feng, Z. Long, Q. Chen, Assessment of various CFD models for predicting airflow and pressure drop through pleated filter system, Build. Environ. 75 (2014) 132–141, http://dx.doi.org/10.1016/j.buildenv.2014.01.022.
[14] B.O. Andersen, CFD modelling of pulse-jet cleaning in fabric filters(Master's thesis) Technical University of Denmark, 2014.
[15] CD-adapco. User Guide STAR-CCM+ Version 8.04, 2013.
[16] J. Ferziger, M. Perić, Computational Methods for Fluid Dynamics, third ed. Springer Limited, London, 2002 (ISBN 9783540420743).
[17] F. White, Viscous Fluid Flow, McGraw-Hill Series in Mechanical Engineering, third ed.McGraw-Hill Higher Education, 2006 (ISBN 9780071244930).
[18] T.H. Shih, W. Liou, A. Shabbir, Z. Yang, J. Zhu, A new k-epsilon eddy viscosity model for high Reynolds number turbulent flows: model development and validation, Technical Report NASA-TM-106721, NASA, 1994.
[19] W. Rodi, Experience with two-layer models combining the k-epsilon model with a one-equation model near the wall, 29th Aerospace Sciences Meeting. AIAA-91-0216, American Institute of Aeronautics and Astronautics, 1991http://dx.doi.org/10.2514/6.1991-216.
[20] S. Sarkar, B. Lakshmanan, Application of a Reynolds stress turbulence model to the compressible shear layer, AIAA J. 29 (5) (1991) 743–749, http://dx.doi.org/10.2514/3.10649.
[21] F.R. Menter, Two-equation eddy-viscosity turbulence models for engineering applications, AIAA J. 32 (8) (1994) 1598–1605, http://dx.doi.org/10.2514/3.12149.
[22] I. Schildermans, J. Baeyens, K. Smolders, Pulse jet cleaning of rigid filters: a literature review and introduction to process modelling, Filtr. Sep. 41 (5) (2004) 26–33, http://dx.doi.org/10.1016/S0015-1882(04)00234-4.
[23] E. Rothwell, Pulse-driven injectors for fabric dust filters III: comparative performance of model and commercial assemblies, Filtr. Sep. 27 (5) (1990) 345–349, http://dx.doi.org/10.1016/0015-1882(90)80366-S.
[24] J. Sievert, F. Löffler, Fabric cleaning in pulse-jet filters, Chem. Eng. Process. Process Intensif. 26 (2) (1989) 179–183, http://dx.doi.org/10.1016/0255-2701(89)90010-X.
[25] T.T. Lim, On the role of Kelvin-Helmholtz-like instability in the formation of turbulent vortex rings, Fluid Dyn. Res. 21 (1) (1997) 47, http://dx.doi.org/10.1016/S0169-5983(96)00059-7.
[26] T. Murugan, S. De, C. Dora, D. Das, Numerical simulation and PIV study of compressible vortex ring evolution, Shock Waves 22 (1) (2012) 69–83, http://dx.doi.org/10.1007/s00193-011-0344-9.
[27] A. Ooi, T. Rochwerger, A. Risborg, C. Harkin, J. Soria, M. Li, et al., Investigation of the flow structures in supersonic free and impinging jet flows, J. Fluids Eng. Trans. ASME 135 (3) (2013)http://dx.doi.org/10.1115/1.4023190.
[28] J. Panda, R.G. Seasholtz, Measurement of shock structure and shock–vortex interaction in underexpanded jets using Rayleigh scattering, Phys. Fluids 11 (12) (1999) 3761–3777, http://dx.doi.org/10.1063/1.870247.

[29] R. Dennis, J. Wilder, D. Harmon, Predicting pressure loss for pulse jet filters, J. Air Pollut. Control Assoc. 31 (9) (1981) 987–992, http://dx.doi.org/10.1080/00022470.1981.10465316.
[30] W. Humphries, J. Madden, Fabric filtration for coal-fired boilers: dust dislodgement in pulse jet filters, Filtr. Sep. 2 (21) (1983) 40–44.
[31] R. Klingel, F. Löffler, Influence of cleaning intensity on pressure drop and residual dust areal density in a pulse jet fabric filter, Filtech conference 1983, pp. 306–314.
[32] P. Chakraborty, R.J. Balachandar, R.J. Adrian, On the relationships between local vortex identification schemes, J. Fluid Mech. 535 (2005) 189–214, http://dx.doi.org/10.1017/S0022112005004726.